Impacts of convection schemes on simulating tropical-temperate troughs over southern Africa

Tomoki Tozuka[1], Babatunde J. Abiodun[2], Francois A. Engelbrecht[3]

[1] Department of Earth and Planetary Science, Graduate School of Science, The University of Tokyo, Tokyo, Japan
[2] Climate System Analysis Group, University of Cape Town, Cape Town, South Africa
[3] CSIR Natural Resources and the Environment, Climate Studies, Modelling and Environmental Health, Pretoria, South Africa

Climate Dynamics

January 2014, Volume 42, Issue 1-2, pp 433-451

The final publication is available at:

http://link.springer.com/article/10.1007%2Fs00382-013-1738-4

Corresponding author address: Tomoki Tozuka, Department of Earth and Planetary Science, Graduate School of Science, The University of Tokyo, 7-3-1 Hongo, Bunkyo-ku, Tokyo 113-0033, Japan. E-mail: tozuka@eps.s.u-tokyo.ac.jp. Tel: +81-3-5841-4288. Fax: +81-3-5841-8791.

Abstract

This study examines southern African summer rainfall and tropical temperate troughs (TTTs) simulated with three versions of an atmospheric general circulation model differing only in the convection scheme. All three versions provide realistic simulations of key aspects of the summer (November-February) rainfall, such as the spatial distribution of total rainfall and the percentage of rainfall associated with TTTs. However, one version has a large bias in the onset of the rainy season. Results from self-organizing map (SOM) analysis on simulated daily precipitation data reveals that this is because the occurrence of TTTs is underestimated in November. This model bias is not related to westerly wind shear that provides favorable conditions for the development of TTTs. Rather, it is related to excessive upper level convergence and associated subsidence over southern Africa.

Furthermore, the model versions are shown to be successful in capturing the observed drier (wetter) conditions over the southern African region during El Niño (La Niña) years. The SOM analysis reveals that nodes associated with TTTs in the southern (northern) part of the domain are observed less (more) often during El Niño years, while nodes associated with TTTs occur more frequently during La Niña years. Also, nodes associated with dry conditions over southern Africa are more (less) frequently observed during El Niño (La Niña) years. The models tend to perform better for La Niña events, because they are more successful in representing the observed frequency of different synoptic patterns.

1. Introduction

Tropical-temperate troughs (TTTs) provide a substantial portion of summer rainfall over southern Africa (Africa south of 12.5°S). During a TTT event, tropical convection is linked with a transient system in the mid-latitudes (e.g. Vigaud et al. 2012), and a band of cloud and rain extending from the northwest to the southeast is formed (Harrison 1984; Todd and Washington 1999; Washington and Todd 1999; Todd et al. 2004; Ratna et al. 2012). The positioning of the Angola Low or related troughs over the northwestern part of the subcontinent plays an important role in the formation of TTTs over southern Africa (Lyon and Mason, 2007, 2009; Vigaud et al. 2008).

The interannual variation of rainfall in this region has been shown to be influenced by El Niño-Southern Oscillation (ENSO) (e.g. Lindesay and Vogel 1990; Richard et al. 2000; Cook 2000, 2001; Manhique et al. 2011) and sea surface temperature (SST) anomalies in the surrounding oceans (e.g. Mason 1995; Rouault et al. 2003; Washington and Preston 2006; Williams et al. 2008; Vigaud et al. 2012), including those associated with the subtropical dipole modes (Reason 2002; Fauchereau et al. 2009; Morioka et al. 2010, 2011, 2012). To mitigate impacts of the above-mentioned interannual variations, skillful predictions are required (Behera and Yamagata 2001; Reason et al. 2006; Landman et al. 2009). Landman and Beraki (2012) conducted retroactive multi-model forecasts over southern Africa, and found that their forecasts had relatively good skill during El Niño and La Niña years, but performed poorly during neutral years (years without either El Niño or La Niña events). Also, Yuan et al. (2013) showed that a coupled general circulation model (CGCM) with high skills in predicting ENSO and the subtropical dipole modes had relatively high skills in predicting southern African precipitation anomalies in a broad region south of 10°S. Although these studies have illustrated some useful skill in forecasting summer rainfall over southern Africa, the simulation and prediction of rainfall over this region still faces numerous deficiencies. For example, Kataoka et al. (2012) showed that almost all CGCMs that participated in the third phase of the Coupled Model Intercomparison Project (CMIP3; Meehl et al. 2007) failed to simulate the relationship between the precipitation anomaly over southern Africa and global SST anomalies. Also, Lyon and Mason (2009) showed that both atmospheric general circulation models (AGCMs) forced by the observed SST and hindcast seasonal forecasts from CGCMs were unable to reproduce atmospheric circulation anomalies over southern Africa during the strong El Niño event of January-March 1998.

Realistic simulations of summer rainfall are important to obtain plausible projections of future climate change over southern Africa, which may in turn be helpful for adaptation (e.g. Thomas et al. 2007). The projection of Engelbrecht et al. (2009) suggested a general decrease in rainfall over southern Africa, but with more frequent occurrence of TTTs over the southeastern part of the subcontinent during mid-summer. The latter resulted from the intensification of the Mascarene High over the southwestern Indian Ocean under global warming. On the other hand, Shongwe et al. (2009) have shown that in the CMIP3 models, the rainfall onset over southern Africa is delayed under global warming, owing to a significant reduction in moisture supply from the southwestern Indian Ocean. Also, Lyon (2009) showed a future drying trend in austral summer rainfall, although this was found to be a model-dependent result, and the experiments of Tadross et al. (2005) indicated that choice of cumulus convection scheme may be regarded as an important source of uncertainty in regional projections of future rainfall over southern Africa. The identification of model biases associated with a particular convection scheme, and the eventual improvement or optimal selection of schemes, may contribute to a reduction in uncertainties associated with the projection of future climate change over this region.

Realistic modeling of the basic climatic state is the first step towards the realistic simulation of interannual variations, accurate seasonal prediction, and more reliable projections of future climate change. However, realistic simulations of the southern African rainfall climatology remain a big challenge, partly because of the interaction of tropical and extra-tropical processes over this region. In this regard, van den Heever et al. (1997) used a regional atmosphere model and successfully simulated many aspects of two TTT events. More recently, several studies have attempted to improve the simulation of the rainfall over southern Africa (Crétat et al. 2012; Ratnam et al. 2012). Crétat et al. (2012) conducted 27 sensitivity experiments using three different kinds of parameterizations for cumulus convection, planetary boundary layer, and microphysics in a regional atmospheric model. Ratnam et al. (2012) compared results from the same regional model, which was forced by observed SSTs or coupled with an ocean mixed-layer model. However, these regional models depend heavily on the lateral boundary conditions provided by global models or reanalysis data, making it somewhat difficult to determine the relative contribution of convection schemes in causing model biases. Therefore, we here analyze three versions of the same AGCM differing only in the convection scheme, in light of obtaining more realistic simulations of precipitation over the southern African region. Such an approach was useful for understanding of precipitation in other regions such as in India (e.g. Singh et al. 2011; Sinha et al. 2012).

This paper is organized as follows. A brief description of the model, convection schemes, data, and methodology is given in the next section. In section 3, we compare seasonal variations in precipitation over the southern African region and TTTs simulated by three versions of our AGCM, and discuss possible causes of model biases. We further evaluate model performances in simulating interannual variations, with a special focus on the relation with ENSO, in section 4. Summary and discussions are provided in the final section.

2. Model, data, and methodology

2.1 Model and data

The AGCM used in this study is the Frontier Atmospheric General Circulation Model (FrAM; Guan et al. 2000). Influences of climate variability related to Indian Ocean Dipole and ENSO on regional climate is relatively well captured by the FrAM (Chakraborty et al. 2005; Yuan et al. 2012). It is the atmospheric component of the University of Tokyo Coupled general circulation model (Tozuka et al. 2006, 2011; Doi et al. 2010). The model equations are solved on 28 hybrid levels in the vertical, from the surface up to 10 hPa level, by using the spectral transform method with triangular truncation at wavenumber 42 (T42). The longwave radiation scheme is based on the multiple parameter random model of Shibata and Aoki (1989) and Shibata (1989). In this scheme, H_2O, CO_2, and O_3 are considered as absorbers of the longwave radiation and the cloud emissivity is estimated as a function of temperature. The shortwave radiation scheme is based on Lacis and Hansen (1974), except for the calculation for partially cloudy skies. Here, H_2O and O_3 are considered as absorbers of the shortwave radiation. The cloud fraction is assumed to be a function of relative humidity and calculated following Slingo and Slingo (1991). The assumption of random overlapping is used for both longwave and shortwave radiation. For the land surface model, we used that of Viterbo and Beljaars (1995). The surface eddy fluxes of momentum, heat, and moisture are calculated using bulk formula (Louis et al. 1982), and the effect of subgrid-scale orography induced by the gravity wave drag is parameterized after Palmer et al. (1986).

For the parameterization of cumulus convection, schemes developed by Kuo (1974), Emanuel (1991), and Tiedtke (1989) are used in this study (see Stensrud, 2007 for a review). Briefly, Kuo (1974) formulated a parameterization in which convective precipitation is proportional to total column moisture convergence and it is regarded as a deep-layer control scheme. The parameterization proposed by Tiedtke (1989) is a mass flux scheme with updraft plume, downdraft plume, and environmental subsidence. Entrainment of the updraft plumes is assumed to be proportional to the large-scale moisture convergence, while downdraft plumes are assumed to start at the level of free sink and proportional to the upward mass flux. The precipitation rate is equal to condensed liquid water in the above plume model. Emanuel (1991) developed a parameterization categorized as a mass flux scheme that takes into account the collective effects of the various subparcels in the cloud. A specified fraction of condensed water from the subparcels falls as precipitation. We call these three experiments FrAM_Kuo, FrAM_Emanuel, and FrAM_Tiedtke, respectively. We note that we do not intend to discuss superiority of a particular scheme in this study. Rather, the three experiments should be considered as sensitivity experiments of a single AGCM. Also, their performance depends on the resolution of the model, and the parameterization of Kuo (1974) tends to perform better with larger grid size (Singh et al. 2011).

This model is integrated from 1981 to 2008 using monthly SST and sea ice cover data from Hurrell et al. (2007). This dataset has been used in the Atmospheric Model Intercomparison Project (AMIP) simulations. For each experiment, five different initial conditions are used to generate five ensemble members, and outputs after 1982 are used for the present analysis. To generate initial conditions, we have spun up the model from a calm and isothermal atmosphere for about three years (the spin-up time varies slightly for the five different ensemble members, being three years for one member with the others 5, 10, 15, and 20 days shorter, respectively), using the monthly climatologies of SSTs as a lower boundary forcing. The CO_2 concentration was set to the AMIP-specified value of 348 ppmv, and the solar constant was set to AMIP-specified 1365 W m^{-2}.

We also use the Global Precipitation Climatology Project (GPCP) data (Adler et al., 2003) for precipitation, and the National Centers for Environmental Prediction (NCEP)/National Center for Atmospheric Research (NCAR) reanalysis data (Kalnay et al., 1996) for wind, sea-level pressure (SLP), temperature, and specific humidity, to validate the model simulations. We note that we obtained qualitatively similar results even when we used the NCEP-DOE reanalysis 2 data (Kanamitsu et al. 2002) and ECMWF reanalysis data (Uppala et al. 2005), instead of the NCEP/NCAR reanalysis data.

2.2 Methodology: Self-organizing maps

To capture synoptic precipitation patterns, we have applied self-organizing map (SOM) analysis (Kohonen 2001) to daily rainfall anomaly data from November to February (Fig. 1). This method has been successfully used to study climate variations (Tozuka et al. 2008; Morioka et al. 2010) and synoptic weather patterns (Nicholls et al. 2010; MacKellar et al. 2010). In this study, we use a software package called SOM_PAK 3.1 (Kohonen et al. 1995), and readers are referred to Kohonen (1982, 2001) for more details about the SOM.

The input data is first prepared from both observed and simulated daily rainfall anomalies, by interpolating the observed data into the T42 grid of the AGCM over the southern African region (43.254°S-12.558°S, 0°-50.625°E). Since the daily rainfall data of the GPCP is available only from 1997 to 2008, we focus on the rainy seasons (November to February) from 1997/98 to 2007/08. As a result, the input matrix consists of 228 grids points with 19 grids in the zonal direction and 12 grids in the meridional direction, and 21120 days of data (1320 days of data for the observations and five ensembles of 1320 days of data for each version of the AGCM). We note that simulated daily precipitation data are used without taking the ensemble mean when we perform the SOM analysis. Then, the dimension of the two-dimensional SOM array is chosen to be 5 nodes x 4 nodes. The topology of the array is selected to be rectangular, and the reference vectors are initialized to random values. We have chosen to use a "bubble" function for the neighborhood function. The training is undertaken in two steps; we use a larger initial learning rate and a neighborhood radius for the first phase to put reference vectors in an order, and a smaller rate and radius to tune the values of reference vectors in the second phase. As a result, we have obtained 20 different daily precipitation patterns, which will be discussed in Sections 3 and 4.

2.3 Methodology: Equitable Threat Score

Skills of the model in simulating interannual variations of precipitation are measured using equitable threat score (ETS), which is defined as

$$ETS = \frac{H - C}{F + A - H - C}$$

(Rogers et al. 1996; Chakraborty and Krishnamurty 2009). Here, F and A are number of grids with simulated and observed precipitation exceeding a specified threshold, respectively, H is the number of grids with both simulated and observed precipitation exceeding the threshold or number of hit, $C = F \cdot A/T$ is the expected number of hit by chance, and T is the total number of grids. Values of ETS may vary from -1/3 to 1 and an ETS of 1 signifies that the simulation is perfect. We calculate the ETS for an area that covers African continent south of 15°S (11.25°E-42.1875°E, 15.348°S-34.883°S).

3. Seasonal variation

The mean precipitation patterns over the southern African region during mid-summer (November-February) are shown in Fig. 2. Areas with high rainfall totals extend southeastward from the equatorial region to around 15°S, and then extend southward along the east coast of Mozambique and South Africa. There is a marked west-east gradient in rainfall over the southern part of the subcontinent, with precipitation less than 2 mm day^{-1} in the southwest. Over eastern South Africa, mid-summer rainfall rates exceed 4 mm day^{-1}. A relatively dry region extends along 20° S, from the western subcontinent towards the east. These observed features are well captured by all three versions of the model. The feature of the dry slot extending eastwards along 20° S, and the precipitation maximum over eastern South Africa, are better captured in FrAM_Tiedtke and FrAM_Kuo. However, the precipitation in the equatorial Africa and the southwestern tropical Indian Ocean to the north of Madagascar is too high in all three versions. Also, the precipitation maximum over northern Madagascar is missing in FrAM_Tiedtke.

Figure 3 shows the mean SLP around the southern African region. All versions provide satisfactory simulations of the relative positions of the subtropical highs in both the South Atlantic and the southern Indian Oceans, and the heat low over the subcontinent. The maximum SLP in St. Helena High is overestimated by 2 hPa, whilst the heat low is simulated to be too deep, by about 5 hPa in all three versions. Since these subtropical highs and the heat low play an important role in the formation and distribution of precipitation over the southern African region (Reason et al. 2006), the model's realistic representation of these highs and the low may be one of the reasons for the reasonably realistic simulation of mid-summer precipitation patterns over the region.

Next, to examine the seasonal evolution of precipitation, observed and simulated monthly mean precipitation patterns are presented in Fig. 4. From May to September, the region is dry in the observations and all three versions. However, by November, the Inter-Tropical Convergence Zone (ITCZ) has progressed to the south of the equator, and precipitation greater than 2 mm day^{-1} occurs over vast areas of the subcontinent. The rainfall maximum over eastern South Africa is linked to that in the tropics by a band-like structure. This large-scale pattern is well-captured in FrAM_Kuo and FrAM_Emanuel, although both of these versions exhibit a wet bias that is particularly strong in the tropics. However, in FrAM_Tiedtke, the precipitation maxima over southern Africa and the tropics are not linked, and the region between 10°S and 25°S is relatively dry. From January to March, most regions are observed to experience precipitation greater than 2 mm day^{-1} with the exception being the dry southwestern subcontinent. The highest rainfall totals occur in a band in the vicinity of 15°S, indicative of the position of the ITCZ. All three versions capture this broad-scale pattern, although the precipitation maximum in March occurs too far south in FrAM_Kuo. The observed feature of a dry slot extending eastward in the observations is well represented in FrAM_Emanuel and FrAM_Tiedtke. In general, the seasonal evolution of rainfall is relatively well captured by all three versions, with the most significant bias in the delayed onset of the rainy season in FrAM_Tiedtke.

To understand the seasonal variation in the rainfall and its biases, it is convenient to check the vertical stability. Following Ninomiya (2008), we have calculated the vertical stability in the 850-500 hPa layer (Fig. 5), which is given by

$$(\theta_{e500} - \theta_{e850})/3.5,$$

where θ_{e500} and θ_{e850} are equivalent potential temperature at 500 and 850 hPa, respectively. In both the observation and the model, the southern African region is convectively unstable from November to March and convectively stable from May to September, in agreement with the rainy season in this region. Furthermore, Fig. 6 shows vertical velocity at 500 hPa. In general, the models are successful in simulating the seasonal march of the vertical velocity. However, the upward motion is too strong in all three versions in the tropics, which may be related to too much precipitation there. Also, upward motion prevails in the southeastern part of South Africa throughout the year in the models, even though downward motion is seen in May and July in the observation. This is related to the wet bias in the southeastern corner of the subcontinent, particularly in FrAM_Kuo.

For quantitative comparison, we have calculated spatial correlation coefficients of rainfall over 0-60°E, 45°S-15°S between the GPCP observations and the three versions of FrAM for each month (Fig. 7). Generally, the correlation coefficients are high for all three versions throughout the year. In particular, the correlation coefficient is higher than 0.79 (0.70) for all months in FrAM_Emanuel (FrAM_Kuo). However, the correlation coefficient takes a minimum in all three versions in November, and as expected from Fig. 4, it becomes lower than 0.5 for FrAM_Tiedtke.

One contributing factor for this dry bias in FrAM_Tiedtke may stem from a bias of simulating subsident conditions over southern Africa in November. Figure 8 shows the velocity potential along with divergent wind at 200 hPa in November. Spuriously strong upper level convergence extends from the southwestern Indian Ocean into the subcontinent in FrAM_Tiedtke, a feature that is likely to inhibit the formation of TTTs during this month. It may also be noted that in FrAM_Emanuel, upper level divergence is simulated over southern Africa, rather than the relatively weak convergence present in FrAM_Kuo and in the observations.

To investigate how well synoptic precipitation patterns are reproduced by the various AGCM versions, and whether the occurrence of TTTs in November is reduced in FrAM_Tiedtke, we have applied the SOM analysis to daily rainfall anomaly data. Twenty different precipitation patterns captured by the SOM are shown in Fig. 9. The precipitation patterns that exhibit marked northwest to southeast alignments over southern Africa, with rainfall rates of more than 4 mm day^{-1} over some areas, are assumed to be associated with the formation of TTTs over this region. Such patterns are found in the bottom row (nodes D1-D5) and left column (nodes A1-D1). We note that our results are not very sensitive to the designation of additional nodes that exhibit some TTT-like characteristics (e.g. node C5), since the qualitative results remains almost the same even if we add or remove one node. The frequency map for both the observation and the model versions (Fig. 10) indicates that all 20 precipitation anomaly patterns seen in the observations are captured by the three versions (since a node with frequency of 0% does not exist in the model frequency maps). The frequency of occurrence of TTT nodes is overestimated by FrAM_Kuo, whilst FrAM_Emanuel and FrAM_Tiedtke provide more realistic representations of these frequencies. Also, as revealed by Figs. 11b, c, d, as much as 70% of simulated precipitation over 30°E-45°E, 15°S-30°S is associated with TTTs. This is in agreement with observations (Fig. 11a). However, FrAM_Kuo exhibits a bias in this regard, in that too high percentage of rainfall over the eastern part of the subcontinent occur in association with TTTs. One possible reason for this bias is that the vertical stability over southern Africa is relatively weak in FrAM_Kuo, especially during the early part of the rainy season, and this may provide more favorable conditions for the development of TTTs in this version of the model (Fig. 5).

Figure 12 shows how frequently each daily precipitation pattern appears each month from November to February. In November, nodes A1-D1 and D2-D5 appear less frequently compared with other months in the observation. This indicates that the occurrence of TTTs is lower during this month. This tendency is exaggerated in FrAM_Tiedtke; nodes D1-D4 appears less frequently in November. Therefore, the model bias as suggested earlier by Figs. 4 and 7 for FrAM_Tiedtke is indeed due to an underestimation in the occurrence of TTT events. Also, nodes that represent TTTs appear too frequently in FrAM_Kuo (also see Fig. 10b) and this explains why it overestimates the percentage of precipitation associated with TTTs (Fig. 11b).

Figure 12 also serves to illustrate the sensitivity of TTT formation in the AGCM to various choices of convection schemes. It is illuminating to investigate whether the differences in the simulated TTT frequencies are due to extra-tropical, or tropical processes. The vertical shear in the zonal wind is displayed in Fig. 13, because westerly shear is known to provide a favorable condition for the development of TTTs (Todd and Washington 1999). Since all three versions show strong westerly shear of about 30 m s^{-1} between 200 hPa and 850 hPa, which is slightly larger than the NCEP/NCAR reanalysis data, model biases in the westerlies do not seem to explain the different simulated frequencies of TTTs, and the less frequent occurrence of TTTs in FrAM_Tiedtke in November. This result suggests that it is primarily the simulated tropical circulation that is sensitive to the choice of convection scheme.

4. Interannual variation

The correlation coefficients between the observed and simulated precipitation anomalies for November-February for the period of 1982-2008 are shown in Fig. 14. In all three versions, the model has the highest skills in the equatorial East Africa, and FrAM_Tiedtke has a correlation coefficient of above 0.6. The precipitation in this region is strongly influenced by the Indian Ocean Dipole (Behera et al. 2005), and it may be relatively easy for the AGCM to reproduce rainfall anomalies forced by anomalous zonal SST gradient across the equatorial Indian Ocean. Also, the correlation coefficient is relatively high in the southern African region with the maximum correlation of 0.4 for FrAM_Kuo and 0.5 for FrAM_Tiedtke and FrAM_Emanuel.

Also, we have evaluated the performance by calculating the ETS for both dry and wet conditions (Fig. 15). In general, the model tends to have higher skill for dry conditions. This is particularly true for FrAM_Tiedtke, which has an ETS of 0.16 with -0.4 and -0.8 mm/day thresholds. Among the three versions, FrAM_Tiedtke has the highest score, except for the 0.0 mm/day threshold for wet conditions. However, the ETS is below 0.2 for all versions regardless of threshold values. This suggests that we need a higher resolution model, or additional model improvements, to more faithfully simulate precipitation anomalies at a grid scale. Indeed, Chakraborty and Krishnamurti (2009) revealed that downscaled forecasts show marked improvements compared with their coarse resolution forecasts for the Indian summer monsoon.

Since the interannual variation in the southern African region is known to be influenced by ENSO (e.g. Lindesay and Vogel 1990; Richard et al. 2000), the difference in the skill levels mentioned above may be closely linked with that of the model to simulate the impacts of ENSO. To examine influences of ENSO, we have defined ENSO years based on the Niño-3.4 index (Fig. 16), which is computed by taking an area-average of SST anomalies over the tropical eastern-central Pacific (120°W-170°W, 5°S-5°N). Here, if the index is above (below) 1 standard deviation, we define the year as an El Niño (a La Niña) year. As a result, we have two El Niño years (1997/98 and 2002/03), three La Niña years (1998/99, 1999/2000, and 2007/08), and six normal years (2000/01, 2001/02, 2003/04, 2004/05, 2005/06, and 2006/07).

Figure 17 shows composites of precipitation anomalies for ENSO years. As has been shown to be typical by previous studies (e.g. Lindesay and Vogel 1990; Richard et al. 2000), the observation shows negative (positive) precipitation anomalies over the southern African region during El Niño (La Niña) years. East Africa exhibits precipitation anomalies opposite to that of the southern African region. This general pattern is well captured by all three versions, but there are some differences between the observation and the simulations. The strongest negative precipitation anomalies during El Niño are found over Mozambique and in Zimbabwe in the observations, but in FrAM_Kuo, wet anomalies extend from the north into Mozambique. In FrAM_Emanuel, the largest negative anomalies occur somewhat to the south than is observed. Although negative precipitation anomalies extend too far into the Indian Ocean, FrAM_Tiedtke simulates the location of largest negative precipitation anomalies over Mozambique relatively well, and this explains why it has the best ETS (Fig. 15a). Also, the strongest positive precipitation anomalies during La Niña is found over Mozambique in the observation, but all versions of the model displaces this maximum to the south over southeastern South Africa. This is why the ETS for the wet conditions tends to be lower compared with that in the dry conditions (Fig. 15b.)

To examine interannual variations in the synoptic precipitation patterns, we have checked how frequently each precipitation pattern appears compared with the climatology during El Niño, normal, and La Niña years in the GPCP observation and three versions of FrAM (Fig. 18). For quantitative comparison of the three versions' performance, phase synchronization (*ps*) is calculated as:

$ps = (n-n')/n *100$

(Misra 1991). Here, *n* is the total number of nodes and *n'* is the number of nodes for which the anomalies in the observation and the model have opposite signs (out of phase). Therefore, $ps = 0$, if signs of anomalies simulated by one version of our AGCM are opposite to those of the GPCP observation for all 20 nodes, and $ps = 100$, if signs of anomalies in a version are consistent with the observation for all 20 nodes.

During El Niño years, nodes associated with TTTs in the southern (northern) part of the domain appear less (more) frequently in the observations; nodes D1-D5 (A1-C1) have negative (positive) anomalies. This is well captured by FrAM_Tiedtke, as is also evident from the fact that this version has the highest phase synchronization among the three versions. However, all versions fail to capture positive anomalies in nodes A2-A5 that show dry conditions over southern Africa. This is one of the reasons why the phase synchronization remains around 50 for the all three versions.

On the other hand, nodes representing TTTs are observed to occur more frequently during La Niña years (note the positive anomalies for nodes A1, B1 and D2-D5 in Fig. 18). FrAM_Emanuel best captures positive anomalies in these nodes with three nodes showing positive anomalies. In contrast to the situation during El Niño years, FrAM_Emanuel and FrAM_Tiedtke tend to perform better in capturing the negative anomalies in Nodes A2-A5. Because these dry patterns appear less frequently, the southern African region experiences more rainfall during La Niña years in general. As a result, FrAM_Emanuel and FrAM_Tiedtke have a high phase synchronization of 70 and 65, respectively, whereas FrAM_Kuo has a low phase synchronization of 45.

As expected in the absence of strong influences from ENSO, the frequency anomaly is within ±1% in more than 80% of the nodes during the normal years. FrAM_Tiedtke (FrAM_Kuo) has the highest (lowest) skill with the phase synchronization of 65 (35).

In summary, the model versions perform better in simulating the interannual variations in the precipitation pattern for La Niña years compared to El Niño or normal years, and FrAM_Emanuel and FrAM_Tiedtke have higher skills in general compared with FrAM_Kuo.

5. Summary and discussions

Using three versions of the same AGCM differing only in the convection scheme, we have evaluated skills of models in simulating southern African rainfall and TTT attributes. All three versions have relatively good capabilities in simulating the summer precipitation, although one version (FrAM_Tiedtke) has a serious bias in the onset. This version simulates excessive upper level convergence and associated subsidence over southern Africa. As a result, development of TTTs is suppressed and connection of tropical and extra-tropical precipitation is delayed by about one month. It is interesting to note that for all three versions, the ability to represent the climatology of monthly rainfall patterns is lowest in November. Since the onset of rainy season is very important for subsistence farming in the southern African region, this model bias is potentially a limiting factor to the skill of early-season seasonal forecasts over the region.

Regarding the simulation of interannual variation, all three versions have relatively good skill, particularly in equatorial East Africa and South Africa. In addition, they are successful in capturing negative (positive) precipitation anomalies over southern Africa in El Niño (La Niña) years, although the exact location of peak precipitation anomalies is slightly shifted. When synoptic precipitation patterns are examined using SOMs, we have found that nodes associated with TTTs in the southern (northern) part of the domain are observed less (more) often during El Niño years. In contrast, nodes associated with TTTs occur more frequently during La Niña years. Also, nodes associated with dry conditions over southern Africa appear more (less) frequently during El Niño (La Niña) years.

Interestingly, the models have better skill in simulating precipitation anomalies during La Niña years, and this may explain why forecast skills have been found to be higher during La Niña years (Landman and Beraki 2012). Because of limitation in the length of daily precipitation data, we note that there are only two (three) El Niño (La Niña) events in the composites, and the analysis should be repeated after the accumulation of observation data.

However, this study is the first to illustrate that the usage of different convection schemes in an AGCM can have pronounced effects on the simulation of southern African rainfall in austral summer. In fact, the study shows that the simulation of upper level circulation and TTT attributes are sensitive to the choice of cumulus convection scheme. We therefore expect that the results presented in this study may shed new light on simulation and prediction of the precipitation over the southern Africa region.

Acknowledgments

Constructive comments from two anonymous reviewers helped us to improve our manuscript. The AGCM was run on the supercomputers of Information Technology Center, the University of Tokyo under the cooperative research with Atmosphere and Ocean Research Institute, the University of Tokyo. The SOM_PAK software was provided by the Neural Network Research Centre at the Helsinki University of Technology and is available at http://www.cis.hut.fi/research/som_pak. The present research is supported by Japan Science and Technology Agency and Japan International Cooperation Agency through Science and Technology Research Partnership for Sustainable Development (SATREPS). The first author is supported by the Japan Society for Promotion of Science through Grant-in-Aid for Exploratory Research 24654150. The second and third authors acknowledge the support from the Applied Centre for Climate and Earth System Studies (ACCESS, South Africa) , and National Research Foundation (NRF, South Africa) in performing this research.

References

Adler RF, Huffman GJ, Chang A, Ferraro R, Xie P-P, Janowiak J, Rudolf B, Schneider U, Curtis S, Bolvin D, Gruber A, Susskind J, Arkin P, Nelkin E (2003) The version 2 Global Precipitation Climatology Project (GPCP) monthly precipitation analysis (1979-Present). J Hydrometeor 4: 1147-1167

Behera SK, Yamagata T (2001), Subtropical SST dipole events in the southern Indian Ocean. Geophys Res Lett 28:327-330

Behera SK, Luo J-J, Masson S, Delecluse P, Gualdi S, Navarra A, Yamagata T (2005) Paramount impact of the Indian Ocean Dipole on the East African short rains: A CGCM study. J Clim 18:4514-4530

Chakraborty A, Behera SK, Mujumdar M, Ohba R, Yamagata T (2005) Diagnosis of tropospheric moisture over Saudi Arabia and influences of IOD and ENSO. Mon Wea Rev 134:598-617

Chakraborty A, Krishnamurti TN (2009) Improving global model precipitation forecasts over India using downscaling and the FSU superensemble. Part II: Seasonal climate. Mon Wea Rev 137:2736-2757

Cook KH (2000) The south Indian convergence zone and interannual rainfall variability over southern Africa. J Clim 13:3789-3804

Cook KH (2001) A Southern Hemisphere wave response to ENSO with implications for southern Africa precipitation. J Atmos Sci 58:2146-2162

Crétat J, Pohl B, Richard Y, Drobinski P (2012) Uncertainties in simulating regional climate of Southern Africa: Sensitivity to physical parameterization using WRF.

Clim Dyn 38:613-634

Doi T, Tozuka T, Yamagata T (2010) The Atlantic Meridional Mode and its coupled variability with the Guinea Dome. J Clim 23:455-475

Emanuel K (1991) A scheme for representing cumulus convection in large-scale models. J Atmos Sci 48:2313-2335

Engelbrecht FA, McGregor JL, Engelbrecht CJ (2009) Dynamics of the conformal cubic atmospheric model projected climate-change signal over southern Africa. Int J Climatol 29:1013-1033

Fauchereau N, Pohl B, Reason CJC, Rouault M, Richard Y (2009) Recurrent daily OLR patterns in the Southern Africa/Southwest Indian Ocean region, implications for South African rainfall and teleconnections. Clim Dyn 32:575-591

Guan Z, Iizuka S, Chiba M, Yamane S, Ashok K, Honda M, Yamagata T (2000) Frontier Atmospheric General Circulation Model version 1.0 (FrAM1.0): Model climatology. Technical Report FTR-1, 27 pp

Harrison MSJ (1984) A generalized classification of South African summer rain-bearing synoptic systems. J Climatol 4:547-560

Hurrell JW, Hack JJ, Shea D, Caron JM, Rosinski J (2008) Sea surface temperature and sea ice boundary dataset for the Community Atmosphere Model. J Clim 21:5145-5153

Kalnay E, Kanamitsu M, Kistler R, Collins W, Deaven D, Gandin L, Iredell M, Saha S, White G, Woollen J, Zhu Y, Leetmaa A, Reynolds R, Chelliah M, Ebisuzaki W, Higgins W, Janowiak J, Mo KC, Ropelewski C, Wang J, Jenne R, Joseph D

(1996) The NCEP/NCAR 40-Year reanalysis project. Bull Amer Meteor Soc 77:437-471

Kanamitsu M, Ebisuzaki W, Woollen J, Yang SK, Hnilo JJ, Fiorino M, Potter GL (2002) NCEP-DOE AMIP-II Reanalysis (R-2). Bull Amer Meteor Soc 83:1631-1643

Kataoka T, Tozuka T, Masumoto Y, Yamagata T (2012) The Indian Ocean subtropical dipole mode simulated in the CMIP3 models. Clim Dyn 39:1385-1399

Kohonen T (1982) Self-organized information of topologically correct features maps. Biol Cyber 43:59-69

Kohonen T, Hynninen J, Kangas J, Laaksonen J (1995) SOM_PAK, The self-organizing map program package version 3.1. Laboratory of Computer and Information Science, Helsinki University of Technology, Finland, 27 pp

Kohonen T (2001) Self-organizing maps, 3rd edn. Springer, Berlin, 501 pp

Kuo HL (1974) Further studies of the parameterization of the influence of cumulus convection on large-scale flow. J Atmos Sci 31:1232-1240

Lacis AA, Hansen JE (1974) A parameterization for the absorption of solar radiation in the earth's atmosphere. J Atmos Sci 31:118-133

Landman WA, Kgatuke MJ, Mbedzi M, Beraki A, Bartman A, du Piesanie A (2009) Performance comparison of some dynamical and empirical downscaling methods for South Africa from a seasonal climate modelling perspective. Int J Climatol 29:1535-1549

Landman WA, Beraki A (2012) Multi-model forecast skill for mid-summer rainfall over southern Africa. Int J Climatol 32:303-314

Lindesay JA, Vogel CH (1990) Historical evidence for Southern Oscillation-southern African rainfall relationships. Int J Climatol 10:679-689

Louis J, Tiedtke M, Geleyn JF (1982) A short history of PBL parameterization at ECMWF. Workshop on Planetary Boundary Layer Parameterization, ECMWF, 59-80

Lyon B, Mason SJ (2007) The 1997-98 summer rainfall season in southern Africa. Part I: Observations. J Clim 20:5134-5148

Lyon B, Mason SJ (2009) The 1997-98 summer rainfall season in southern Africa. Part II: Model simulations and coupled model forecasts. J Clim 22:3802-3818

Lyon B (2009) Southern Africa summer drought and heat waves: Observations and coupled model behavior. J Clim 22:6033-6046

MacKellar N, Tadross M, Hewitson B (2010) Synoptic-based evaluation of climatic response to vegetation changes over southern Africa. Int J Climatol 30:774-789

Manhique AJ, Reason CJC, Rydberg L, Fauchereau N (2011) ENSO and Indian Ocean sea surface temperatures and their relationships with tropical temperate troughs over Mozambique and the southwest Indian Ocean. Int J Climatol 31:1-13

Mason, SJ (1995) Sea-surface temperature-South African rainfall associations, 1910-1989. Int J Climatol 15:119-135

Meehl GA, Covey C, Delworth T, Latif M, McAvaney B, Mitchell JFB, Stouffer KJ, Taylor KE (2007) The WCRP CMIP3 multimodel dataset: A new era in climate change research. Bull Amer Meteor Soc 88:1383-1394

Misra J (1991) Phase synchronization. Info Process Lett 38:101-105

Morioka Y, Tozuka T, Yamagata T (2010) Climate variability in the southern Indian Ocean as revealed by self-organizing maps. Clim Dyn 35:1075-1088

Morioka Y, Tozuka T, Yamagata T (2011) On the growth and decay of the subtropical dipole mode in the South Atlantic. J Clim 24:5538-5554

Morioka Y, Tozuka T, Yamagata T (2012) Subtropical dipole modes simulated in a coupled general circulation model. J Clim 25:4029-4047

Nicholls N, Uotila P, Alexander L (2010) Synoptic influences on seasonal, interannual and temperature variations in Melbourne, Australia. Int J Climatol 30:1372-1381

Ninomiya K (2008) Similarities and differences among the South Indian Ocean convergence zone, North American convergence zone, and other subtropical convergence zone simulated using an AGCM. J Meteor Soc Jpn 86:141-165

Palmer TN, Shutts GJ, Swinbank R (1986) Alleviation of systematic westerly bias in general circulation and numerical weather prediction models through an orographic gravity wave drag parameterization. Quat J Roy Meteor Soc 112: 1001-1039

Ratna SB, Behera S, Ratnam JV, Takahashi K, Yamagata T (2012), An index for tropical temperate troughs over southern Africa. Clim Dyn. doi:10.1007/s00382-012-1540-8

Ratnam JV, Behera SK, Masumoto Y, Takahashi K, Yamagata T (2012) A simple regional coupled model experiment for summer-time climate simulation over southern Africa. Clim Dyn 39:2207-2217

Reason CJC (2002) Sensitivity of the southern African circulation to dipole sea-surface temperature patterns in the south Indian Ocean. Int J Climatol 22:377-393

Reason CJC, Landman W, Tennant W (2006) Seasonal to decadal prediction of southern African climate and its link with variability of the Atlantic Ocean. Bull Amer Meteor Soc 87:941-955

Richard Y, Trzaska, Roucou P, Rouault M (2000) Modification of the southern African rainfall variability/ENSO relationship since the late 1960s. Clim Dyn 16:883-895

Rouault M, Florenchie P, Fauchereau N, Reason CJC (2003) South East tropical Atlantic warm events and southern African rainfall. Geophys Res Lett 30. 8009, doi:10.1029/2002GL014840

Rogers E, Black TL, Deaven DG, DiMego GJ, Zhao Q, Baldwin M, Junker NW, Lin Y (1996) Changes to the operational “early” Eta analysis/forecast system at the National Centers for Environmental Prediction. Wea Forecasting 11:391-413

Shibata K (1989) An economical scheme for the vertical integral of atmospheric emission in longwave radiation transfer. J Meteor Soc Japan 67:1047-1055

Shibata K, Aoki T (1989) An infrared radiative scheme for the numerical models of weather and climate. J Geophys Res 94:14923-14943

Shongwe ME, van Oldenborgh GJ, van der Hurk BJJM, de Boer B, Coelho CAS, van Aalst MK (2009) Projected changes in mean and extreme precipitation in Africa under global warming. Part I: Southern Africa. J Clim 22:3819-3837

Singh AP, Singh RP, Raju PVS, Bhatla R (2011) The impact of three different cumulus parameterizations schemes on the Indian summer monsoon circulation. Int J Clim Ocean Sys 2:27-44

Sinha P, Mohanty UC, Kar SC, Dash SK, Kumari S (2012) Sensitivity of the GCM driven summer monsoon simulations to cumulus parameterization schemes in nested RegCM3. Theor Appl Climatol. doi:10.1007/s00704-012-0728-5

Slingo A, Slingo JM (1991) Response of the National Center for Atmospheric Research Community Climate Model to improvements in the representation of clouds. J Geophys Res 96:15341-15357

Stensrud DJ (2007) Parameterization schemes: Keys to understanding numerical weather prediction models. Cambridge University Press, New York, 459 pp

Tadross, M, Jack C, Hewitson B (2005) On RCM-based projections of change in southern African summer climate. Geophys Res Lett 32. L23713, doi:10.1029/2005GL024460

Thomas DSG, Twyman C, Osbahr H, Hewitson B (2007) Adaptation to climate change and variability: Farmer responses to intra-seasonal precipitation trends in South Africa. Climatic Change 83:301-322

Tiedtke M (1989) A comprehensive mass flux scheme for cumulus parameterization in large-scale models. Mon Wea Rev 117:1779-1800

Todd M, Washington R (1999) Circulation anomalies associated with tropical-temperate troughs in southern Africa and the south west Indian Ocean. Clim Dyn 15:937-951

Todd MC, Washington R, Palmer PI (2004) Water vapour transport associated with tropical-temperate trough systems over southern Africa and the southwest Indian Ocean. Int J Climatol 24:555-568

Tozuka T, Miyasaka T, Chakraborty A, Mujumdar M, Behera SK, Masumoto Y, Nakamura H, Yamagata T (2006) University of Tokyo Coupled General Circulation Model (UTCM1.0). Ocean-Atmos Res Rep 7, 44 pp

Tozuka T, Luo JJ, Masson S, Yamagata T (2008) Tropical Indian Ocean variability revealed by self-organizing maps. Clim Dyn 31:333-343

Tozuka T, Doi T, Miyasaka T, Keenlyside N, Yamagata T (2011) Key factors in simulating the equatorial Atlantic zonal SST gradient in a coupled GCM. J Geophys Res 116. C06010, doi:10.1029/2010JC006717

Uppala SM et al (2005) The ERA-40 re-analysis. Q J R Meteor Soc 131:2961-3012

Van den Heever SC, D'Abreton PC, Tyson PD (1997) Numerical simulation of tropical-temperate troughs over southern Africa using the CSU RAMS model. South African J Sci 93:359-365

Vigaud N, Richard Y, Rouault M, Fauchereau N (2008) Moisture transport between the South Atlantic Ocean and southern Africa: Relationships with summer rainfall and associated dynamics. Clim Dyn 32:113-123

Vigaud N, Pohl B, Crétat J (2012) Tropical-temperate interactions over southern Africa simulated by a regional climate model. Clim Dyn 39:2895-2916

Viterbo P, Beljaars ACM (1995) An improved land surface parameterization scheme in the ECMWF model and its validation. J Clim 8:2716-2748

Washington R, Todd M (1999) Tropical-temperate links in southern African and southwest Indian Ocean satellite-derived daily rainfall. Int J Climatol 19: 1601-1616

Washington R, Preston A (2006) Extreme wet years over southern Africa: Role of Indian Ocean sea surface temperature. J Geophys Res 111. D15104, doi:10.1029/2005JD006724

Williams CJR, Kniveton DR, Layberry R (2008) Influence of South Atlantic sea surface temperatures on rainfall variability and extremes over southern Africa. J Clim 21: 6498-6520

Yuan C, Tozuka T, Yamagata T (2012) IOD Influence on the early winter Tibetan plateau snow cover: Diagnostic analyses and an AGCM simulation. Clim Dyn 39:1643-1660

Yuan C, Tozuka T, Luo JJ, Yamagata T (2013) Predictability of the Subtropical Dipole Modes in a coupled ocean-atmosphere model. Clim Dyn. doi:10.1007/s00382-013-1704-1

Figure captions:

Figure 1: Schematic diagram showing how the SOM is applied.

Figure 2: Mean precipitation (in mm day^{-1}) around the southern African region during the rainy season (November-February) in (a) GPCP, (b) FrAM_Kuo, (c) FrAM_Emanuel, and (d) FrAM_Teidtke.

Figure 3: Mean sea level pressure (in hPa) during the rainy season (November-February) in (a) GPCP, (b) FrAM_Kuo, (c) FrAM_Emanuel, and (d) FrAM_Teidtke.

Figure 4: As in Fig. 2, but for monthly climatology of precipitation (in mm day^{-1}) in January, March, May, July, September, and November.

Figure 5: As in Fig. 4, but for the vertical stability (in K (100 hPa)$^{-1}$).

Figure 6: As in Fig. 4, but for the vertical velocity (in Pa s^{-1}).

Figure 7: Spatial correlation coefficient of rainfall over 0°-60°E, 45°S-15°S between the GPCP observation and three versions of FrAM. All pattern correlation coefficients are significant at 99% confidence level when tested by the Monte Carlo method.

Figure 8: Velocity potential (in m^2 s^{-1} as shown in the color bar) and divergent wind (in m s^{-1} and its magnitude shown in the vector below the color bar) at 200 hPa in November for (a) the NCEP/NCAR reanalysis data, (b) FrAM_Kuo, (c) FrAM_Emanuel, and (d) FrAM_Tiedtke.

Figure 9: SOM array of daily rainfall anomalies (in mm day^{-1}). Each node represents a synoptic precipitation pattern over the southern African region.

Figure 10: Frequency map of the SOM array showing how frequently each precipitation pattern appears during the rainy season (November-February).

Figure 11: As in Fig. 2, but for percentage of precipitation in the rainy season (November-February) associated with nodes representing TTTs.

Figure 12: (First row) Frequency map of the SOM array showing how frequently each precipitation pattern appears from November to February in the observation. (Second, third, and fourth rows) Model biases in frequency of each precipitation pattern in FrAM_Kuo, FrAM_Emanuel, and FrAM_Tiedtke, respectively. Positive (Negative) values signify that the pattern appears more (less) frequently compared with the observation.

Figure 13: As in Fig. 2, but for the zonal wind shear (200-850 hPa; m s^{-1}) in November.

Figure 14: Correlation coefficients between the observed and simulated precipitation in the southern African region for November-February for the period of 1982-2008: (a) FrAM_Kuo, (b) FrAM_Emanuel, and (c) FrAM_Tiedtke.

Figure 15: Equitable threat score of precipitation during November-February of the period of 1982-2008 for (a) dry and (b) wet conditions.

Figure 16: Normalized time series of Niño-3.4 index in November-February.

Figure 17: Composite of precipitation anomalies (in mm day^{-1}) in (upper panels) El Niño and (lower panels) La Niña years.

Figure 18: Frequency map of the SOM array showing how frequently each precipitation pattern appears during El Niño, normal, and La Niña years in the GPCP observation and three versions of FrAM. Here, deviations from the

seasonal mean percentage are shown, and “ps” signifies phase synchronization.

717 **Figures**

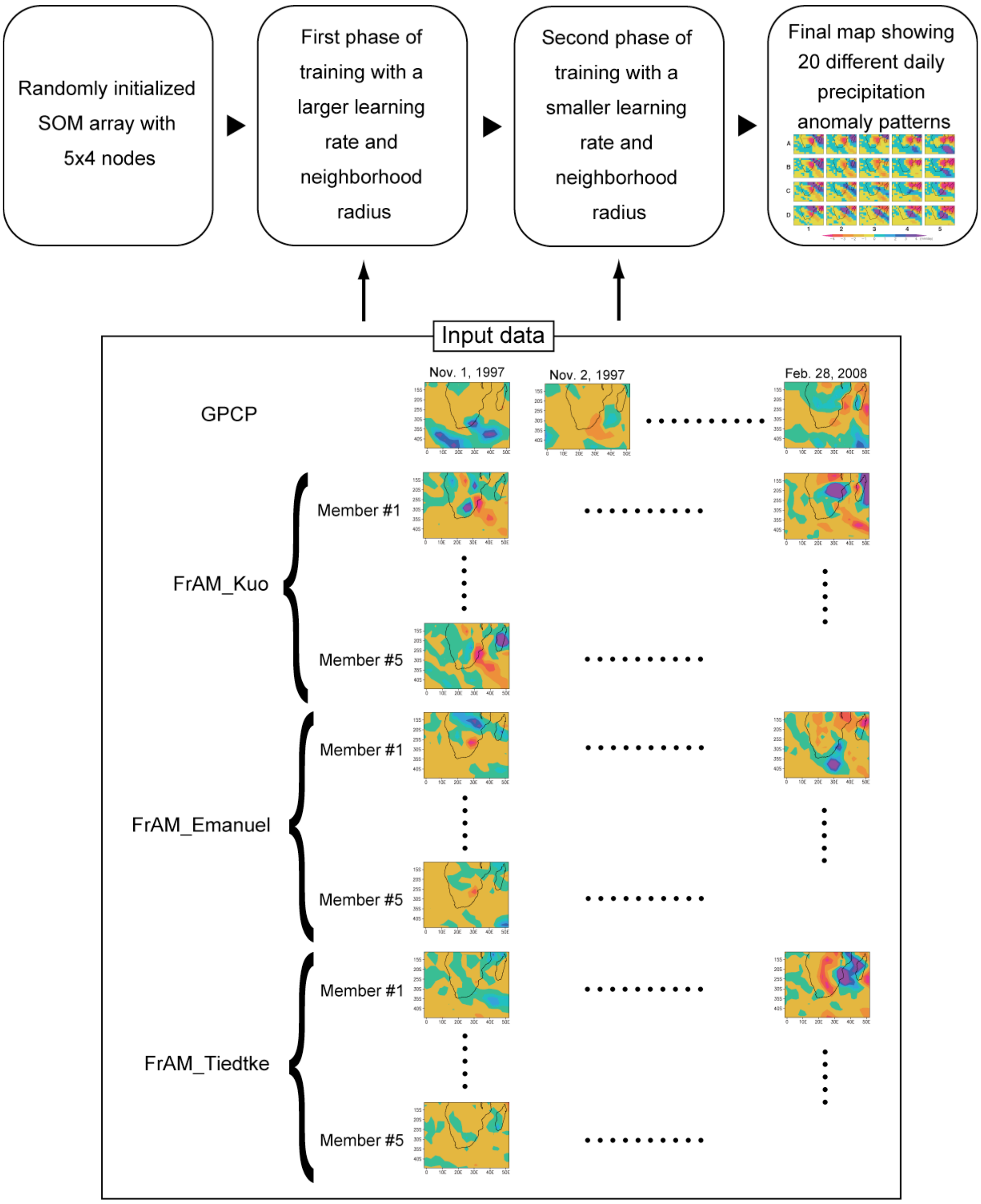

718

719 **Figure 1:** Schematic diagram showing how the SOM is applied.

720

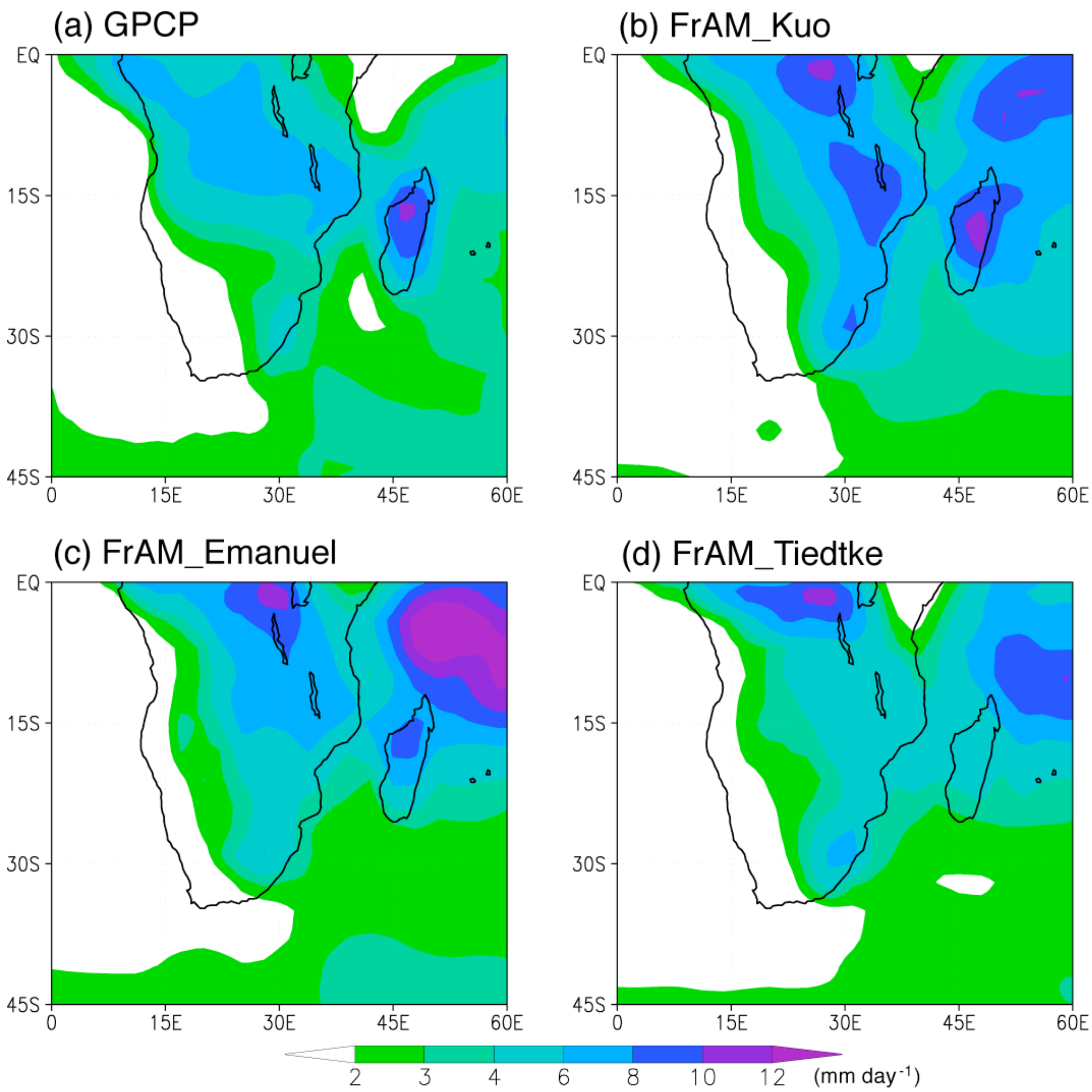

Figure 2: Mean precipitation (in mm day^{-1}) around the southern African region during the rainy season (November-February) in (a) GPCP, (b) FrAM_Kuo, (c) FrAM_Emanuel, and (d) FrAM_Teidtke.

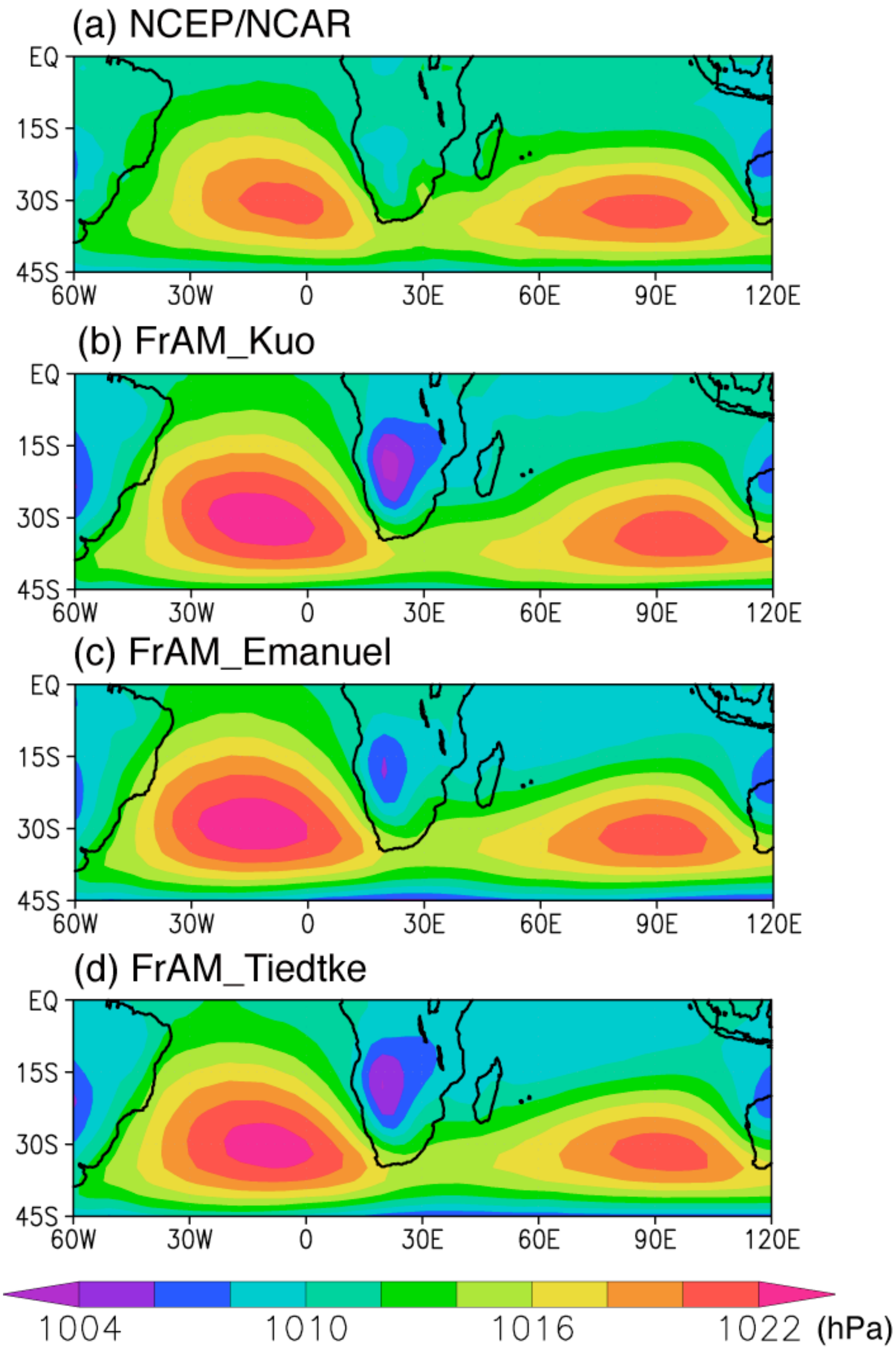

Figure 3: Mean sea level pressure (in hPa) during the rainy season (November-February) in (a) GPCP, (b) FrAM_Kuo, (c) FrAM_Emanuel, and (d) FrAM_Teidtke.

732

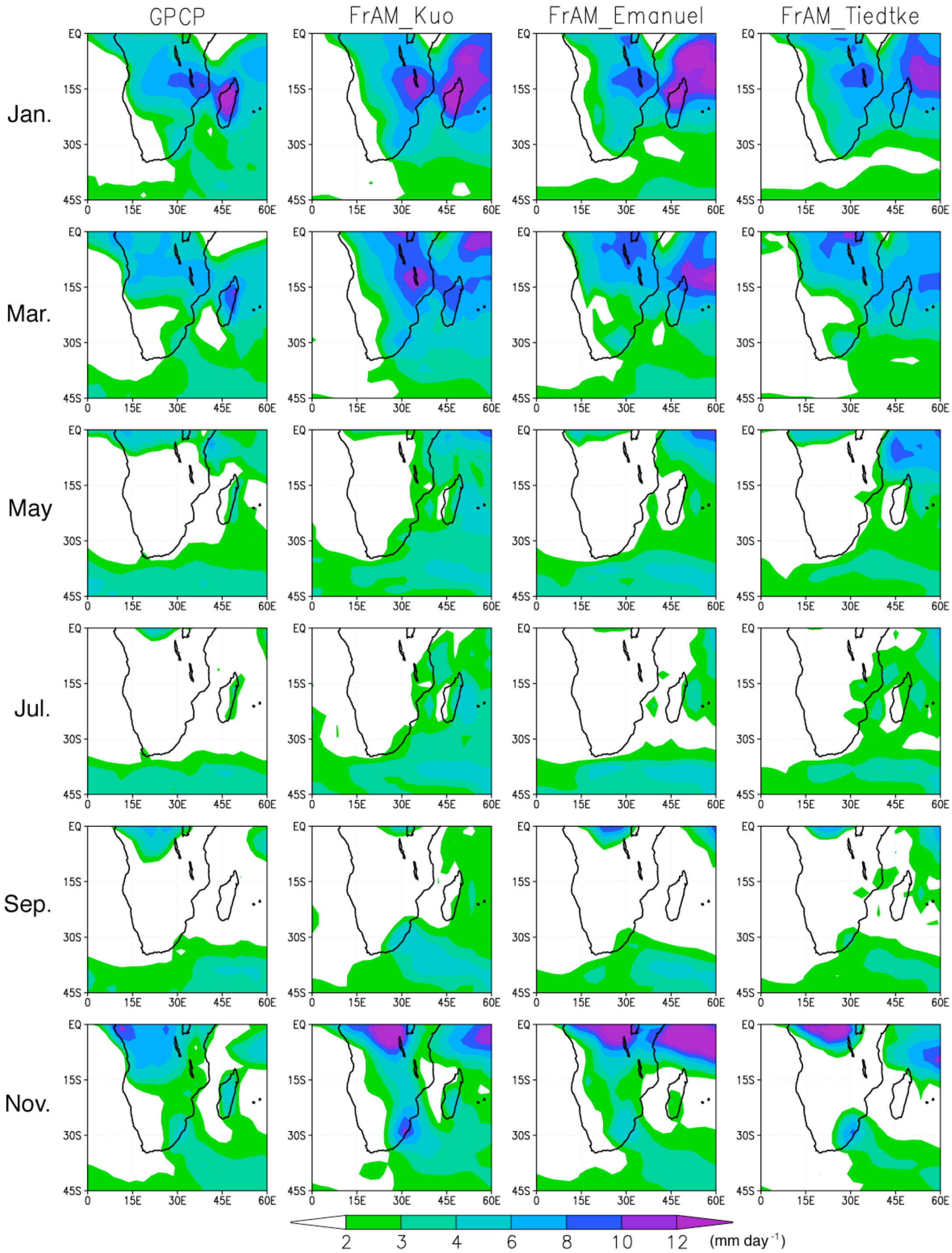

733

734 **Figure 4:** As in Fig. 2, but for monthly climatology of precipitation (in mm day^{-1}) in

735 January, March, May, July, September, and November.

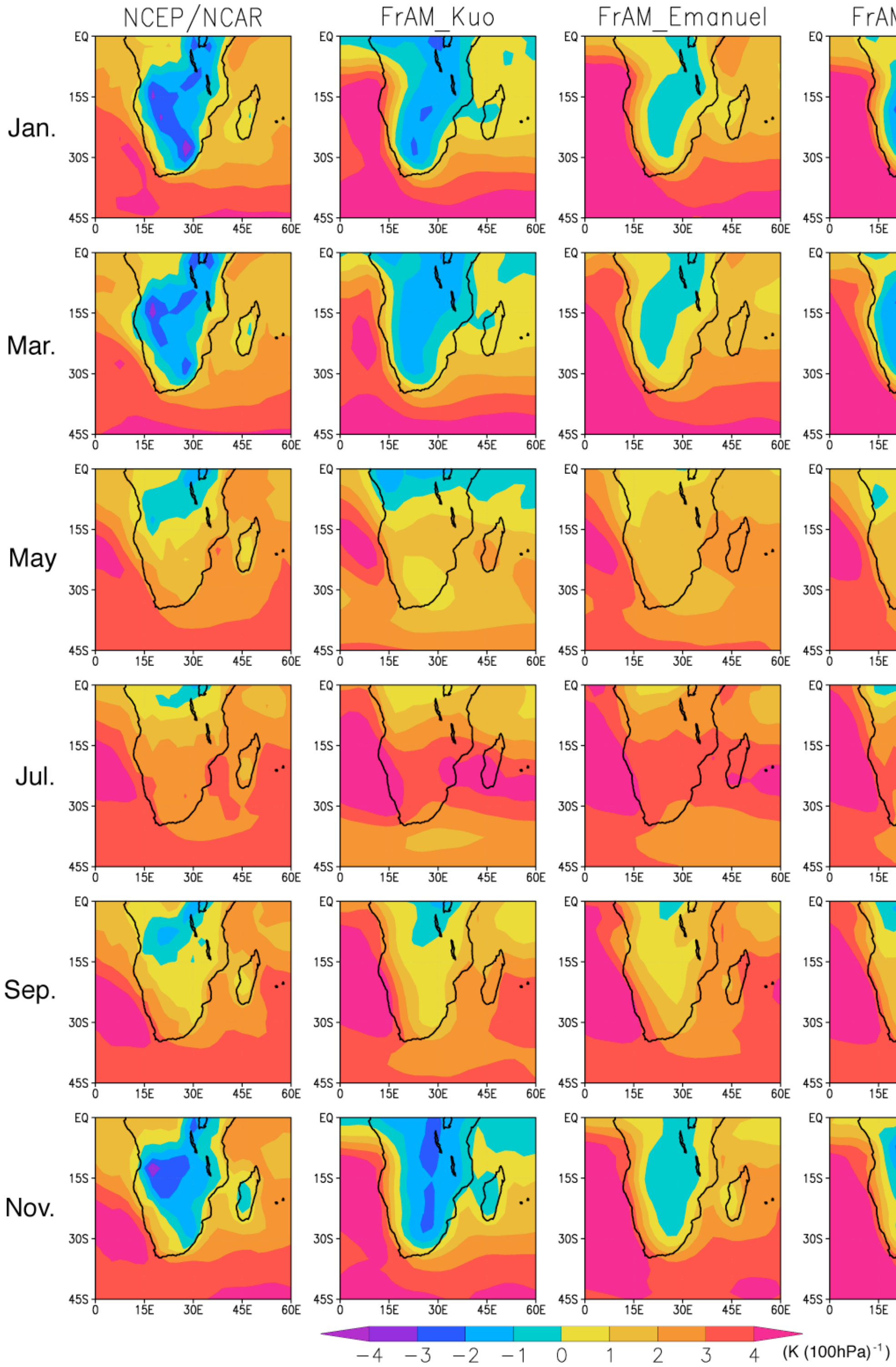

Figure 5: As in Fig. 4, but for the vertical stability (in K (100 hPa)$^{-1}$).

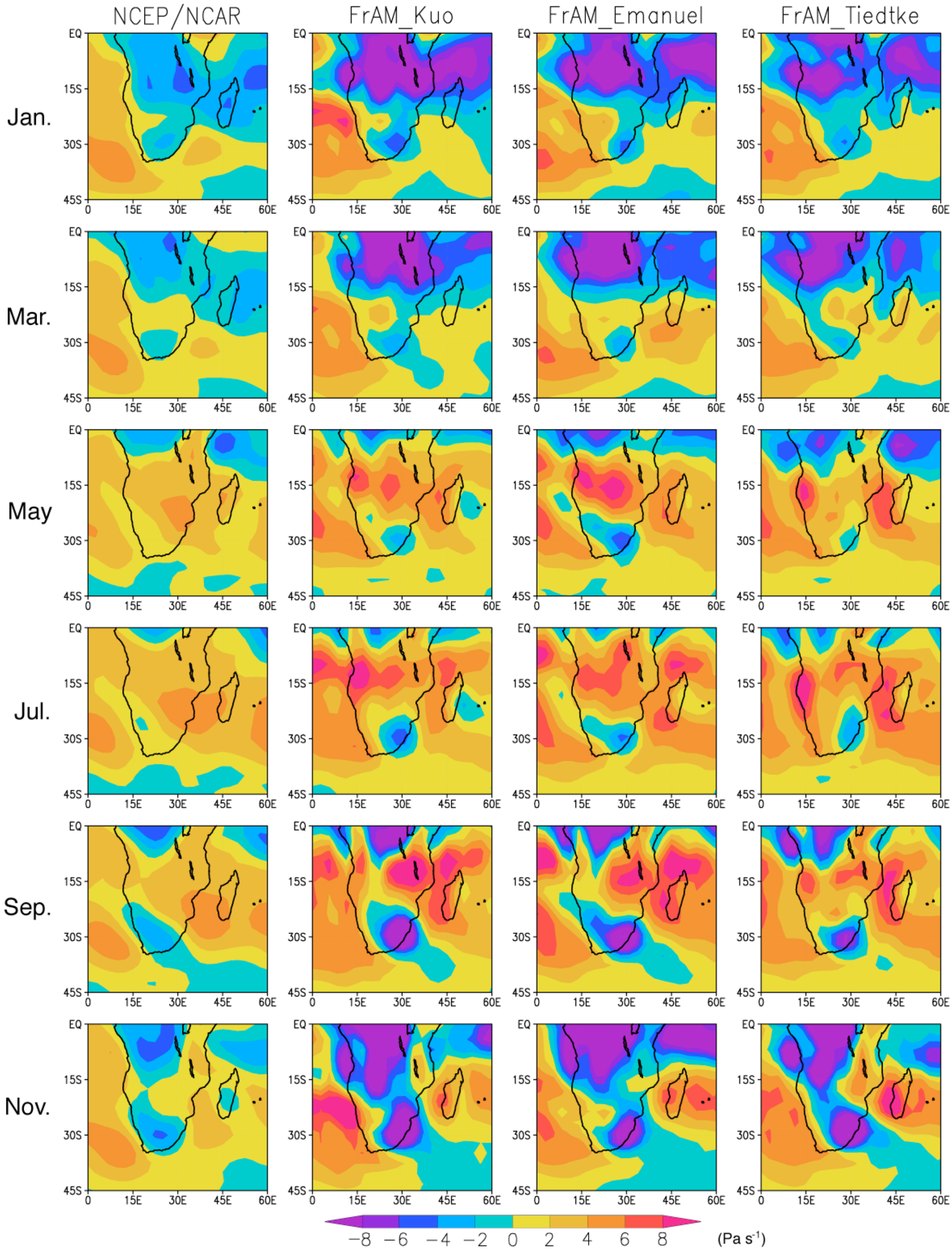

738

739 **Figure 6:** As in Fig. 4, but for the vertical velocity (in Pa s^{-1}).

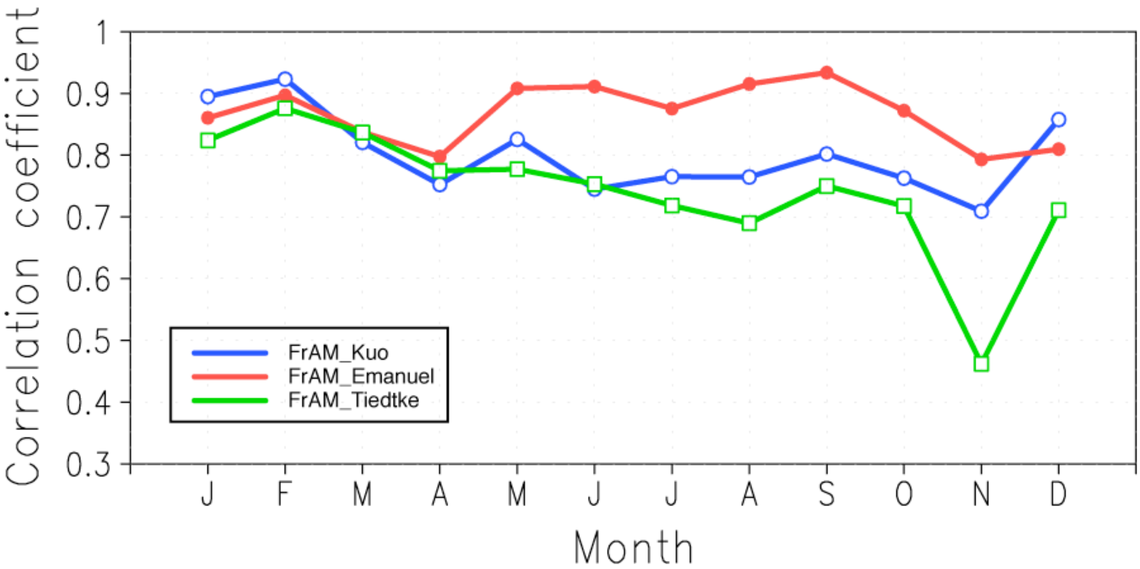

Figure 7: Spatial correlation coefficient of rainfall over 0°-60°E, 45°S-15°S between the GPCP observation and three versions of FrAM. All pattern correlation coefficients are significant at 95% confidence level when tested by the Monte Carlo method.

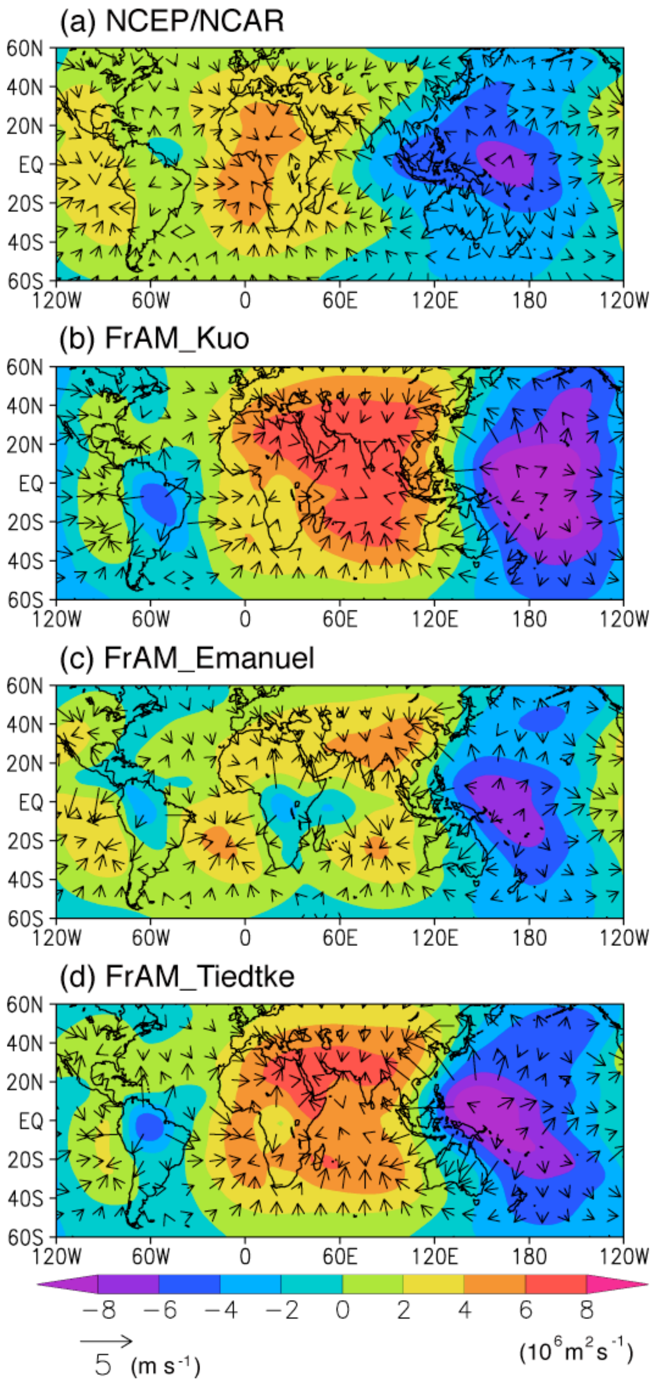

Figure 8: Velocity potential (in $m^2\ s^{-1}$ as shown in the color bar) and divergent wind (in $m\ s^{-1}$ and its magnitude shown in the vector below the color bar) at 200 hPa in November for (a) the NCEP/NCAR reanalysis data, (b) FrAM_Kuo, (c) FrAM_Emanuel, and (d) FrAM_Tiedtke.

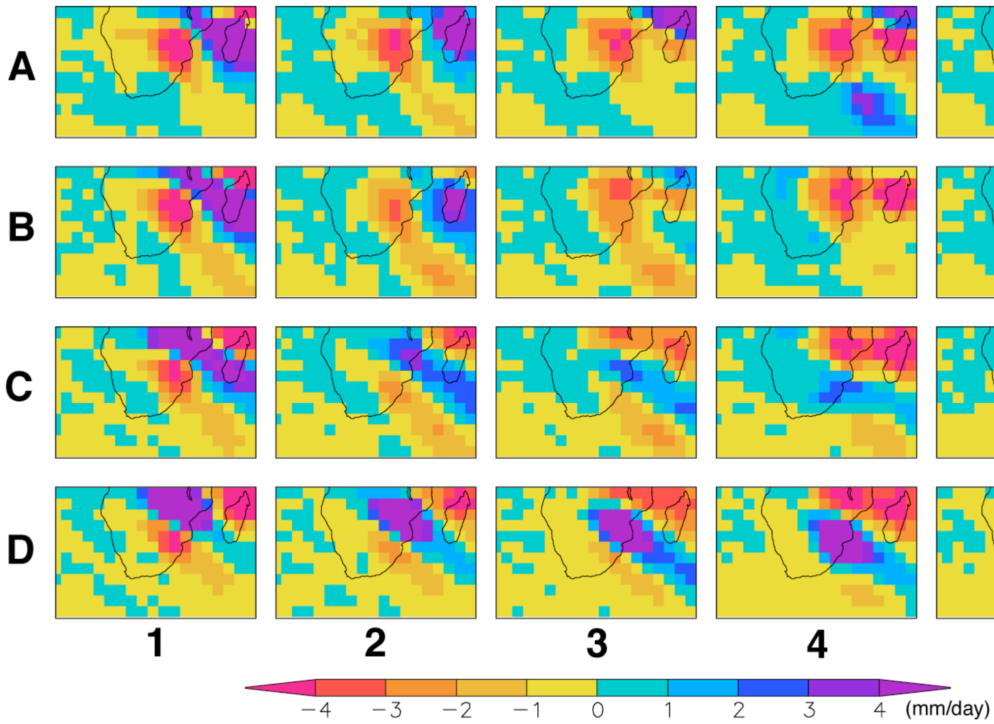

Figure 9: SOM array of daily rainfall anomalies (in mm day^{-1}). Each node represents a synoptic precipitation pattern over the southern African region.

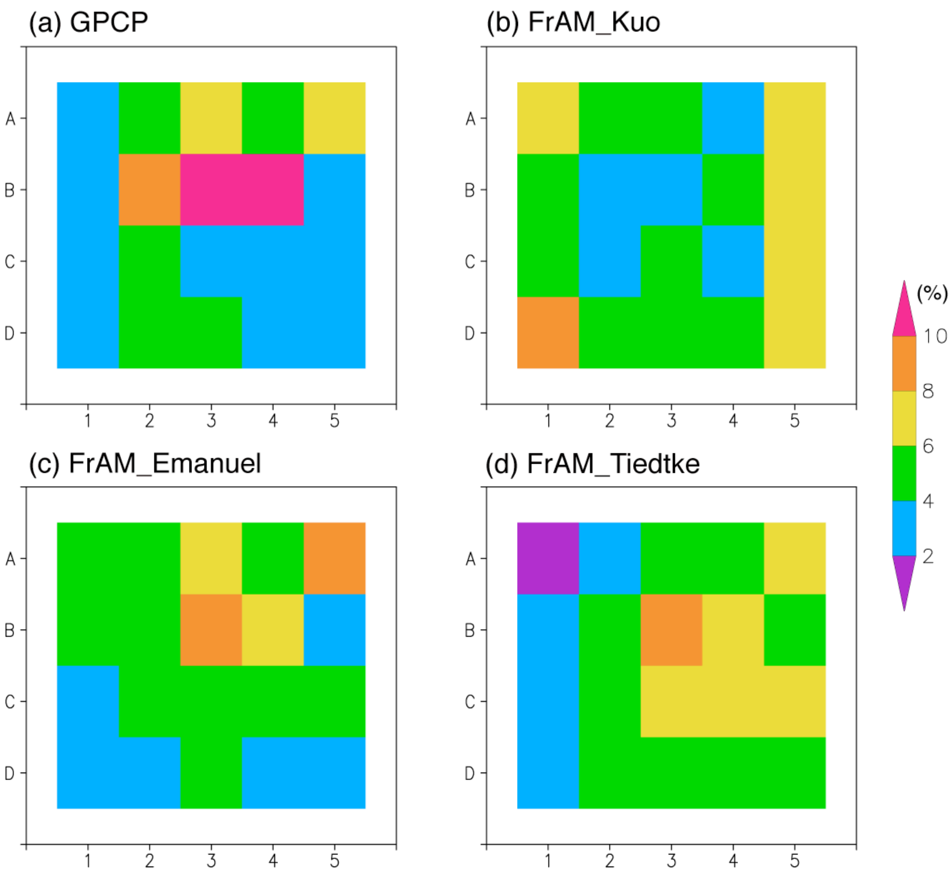

Figure 10: Frequency map of the SOM array showing how frequently each precipitation pattern appears during the rainy season (November-February).

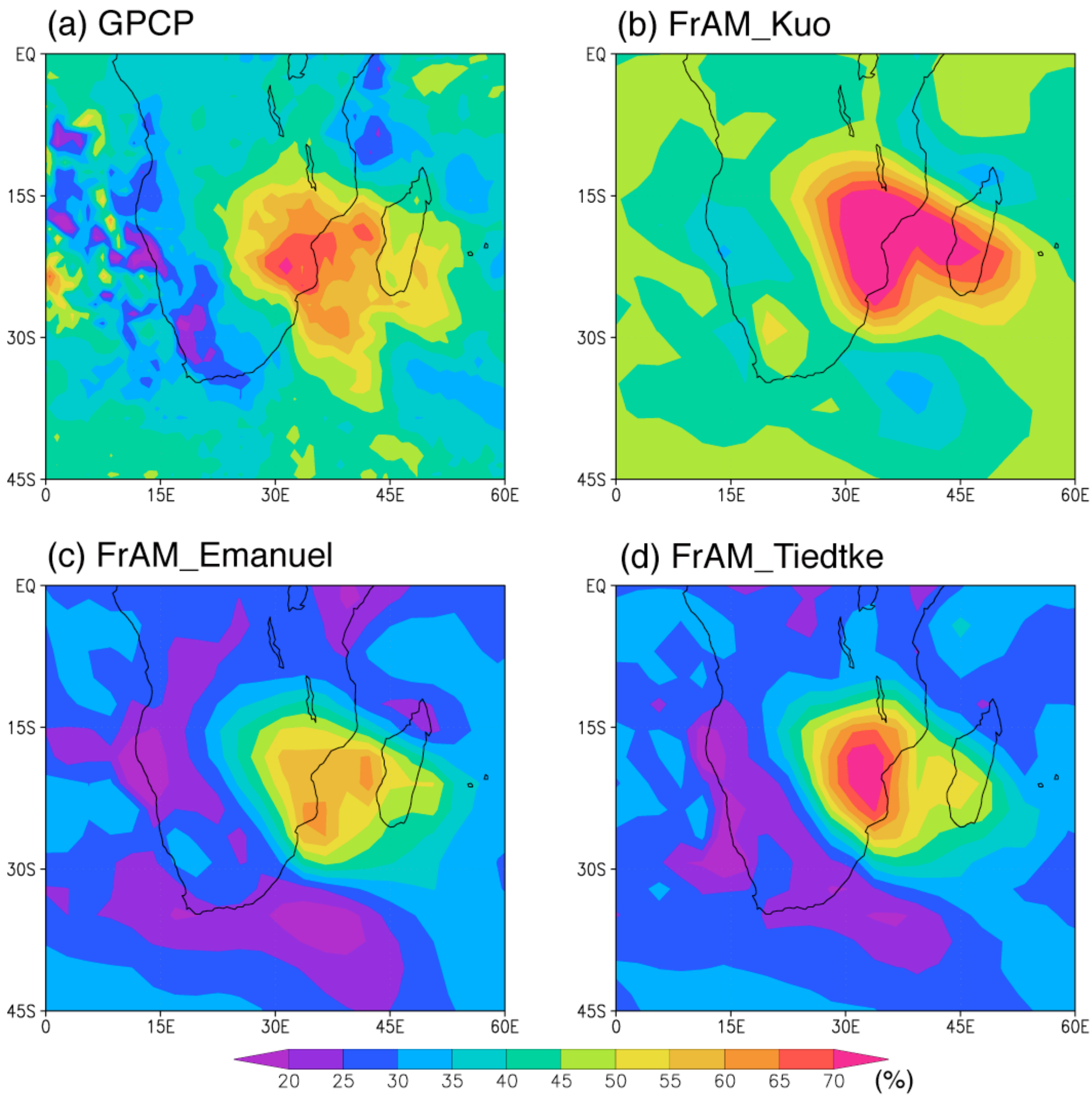

Figure 11: As in Fig. 2, but for percentage of precipitation in the rainy season (November-February) associated with nodes representing TTTs.

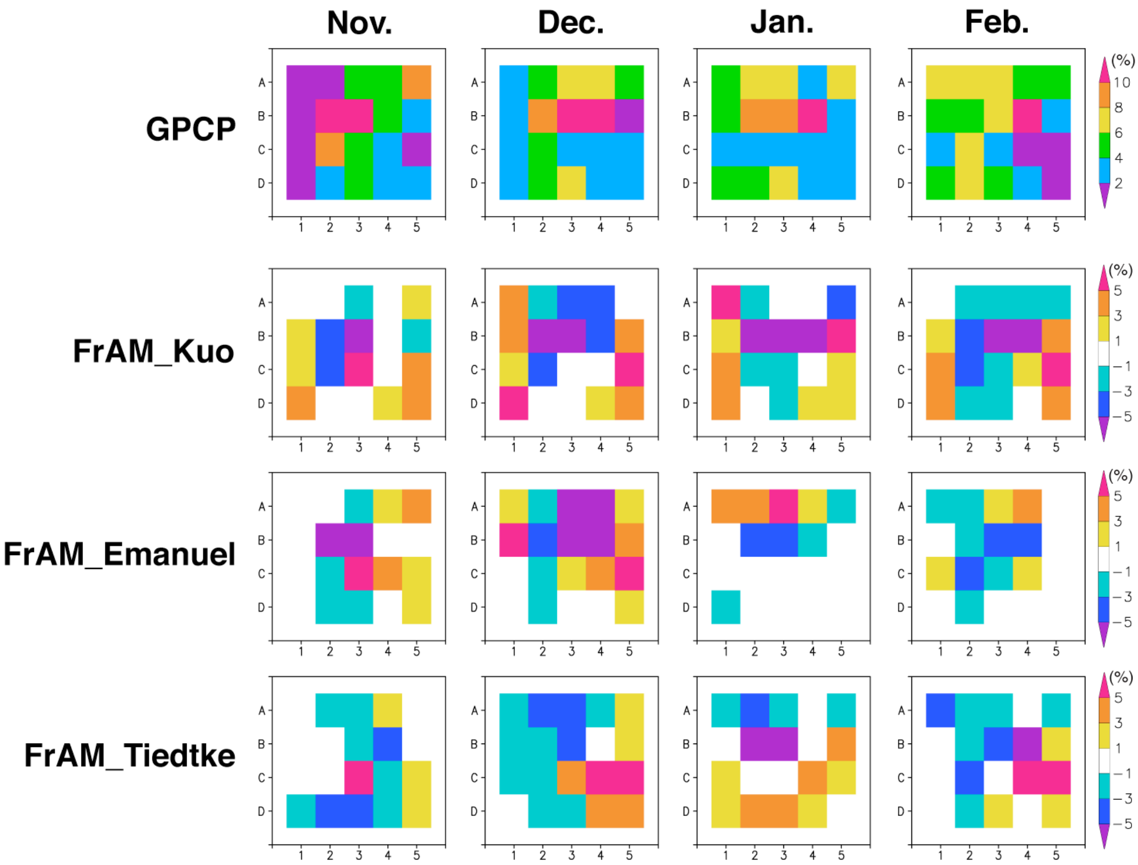

Figure 12: (First row) Frequency map of the SOM array showing how frequently each precipitation pattern appears each month from November to February in the observation. (Second, third, and fourth rows) Model biases in frequency of each precipitation pattern in FrAM_Kuo, FrAM_Emanuel, and FrAM_Tiedtke, respectively. Positive (Negative) values signify that the pattern appears more (less) frequently compared with the observation.

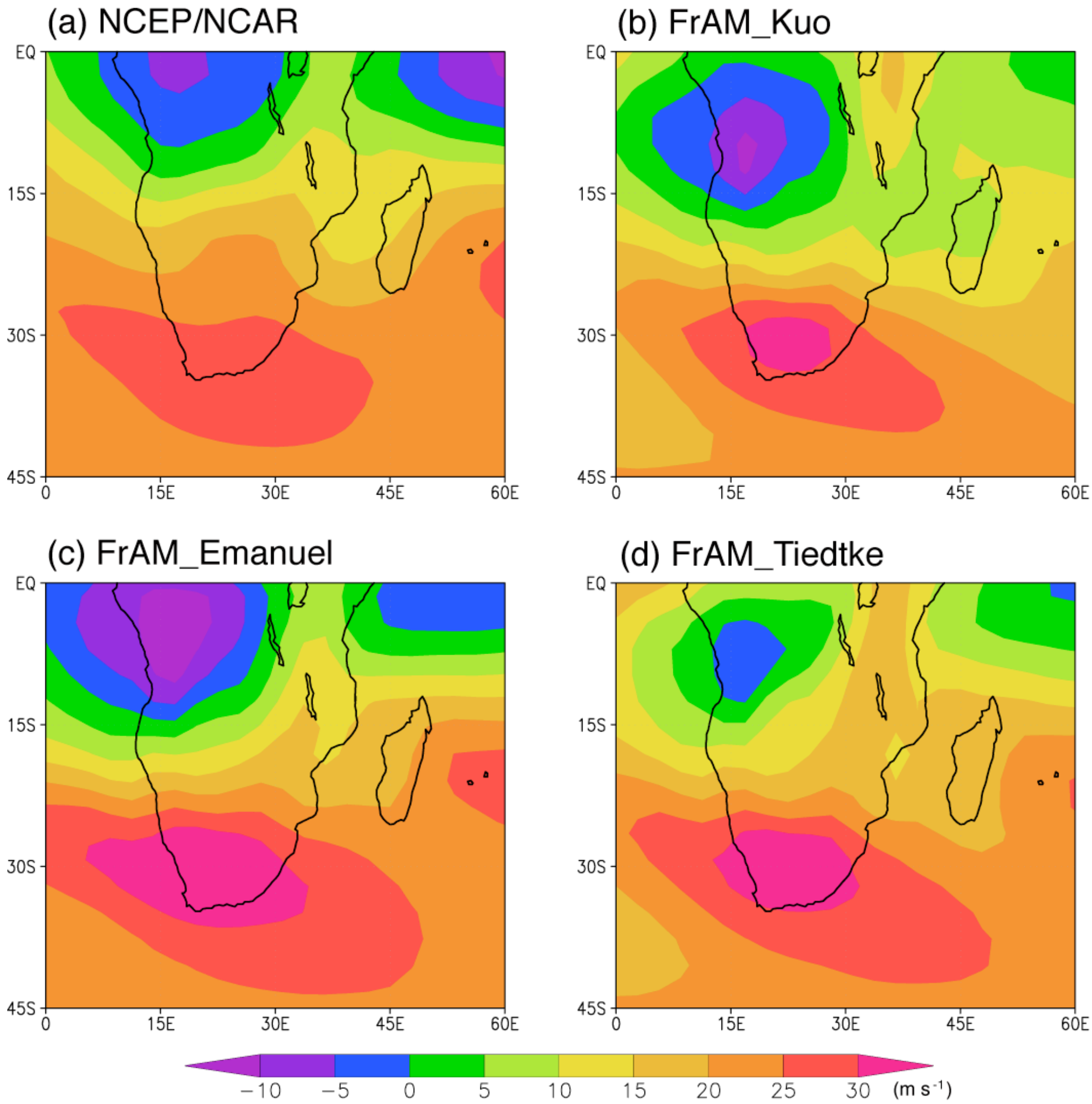

Figure 13: As in Fig. 2, but for the zonal wind shear (200-850 hPa; m s^{-1}) in November.

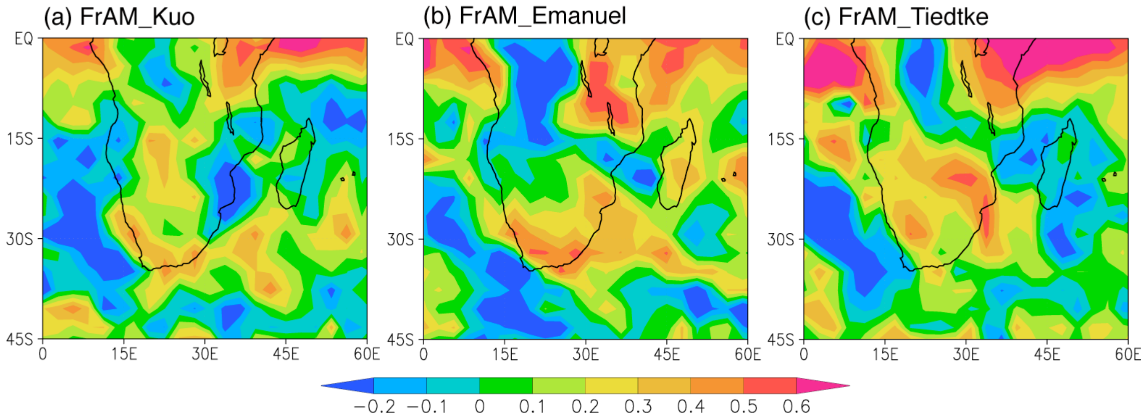

Figure 14: Correlation coefficients between the observed and simulated precipitation in the southern African region for November-February for the period of 1982-2008: (a) FrAM_Kuo, (b) FrAM_Emanuel, and (c) FrAM_Tiedtke.

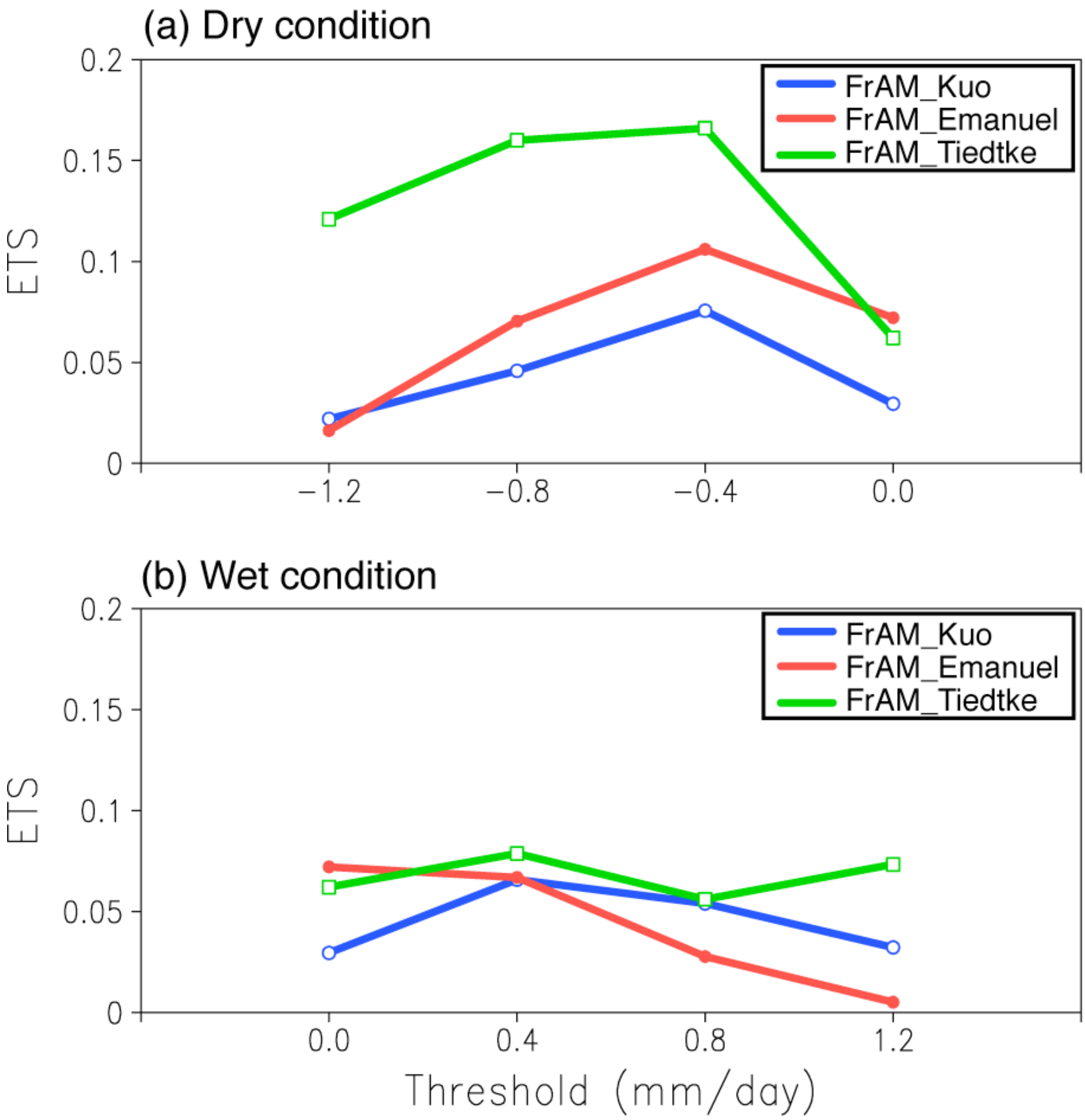

Figure 15: Equitable threat score of precipitation during November-February of the period of 1982-2008 for (a) dry and (b) wet conditions.

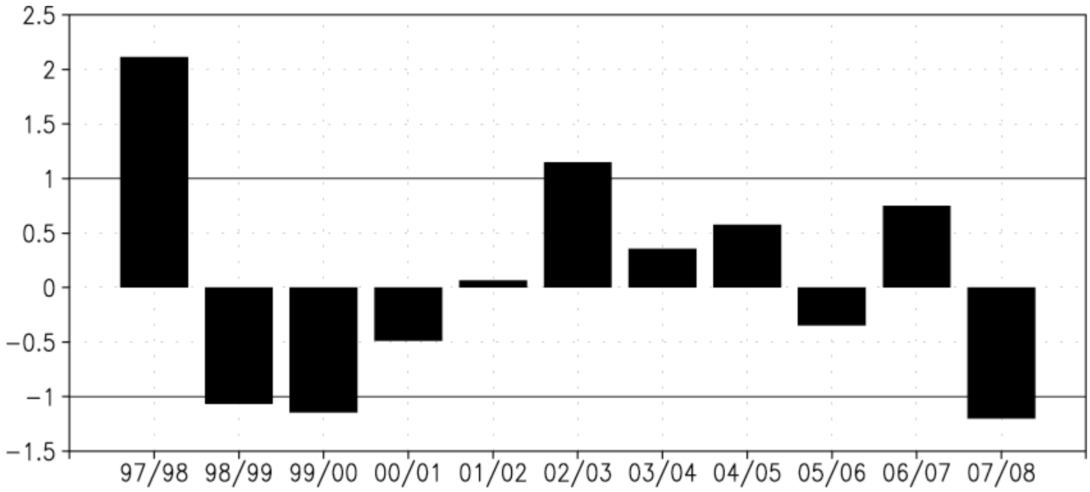

Figure 16: Normalized time series of Niño-3.4 index in November-February.

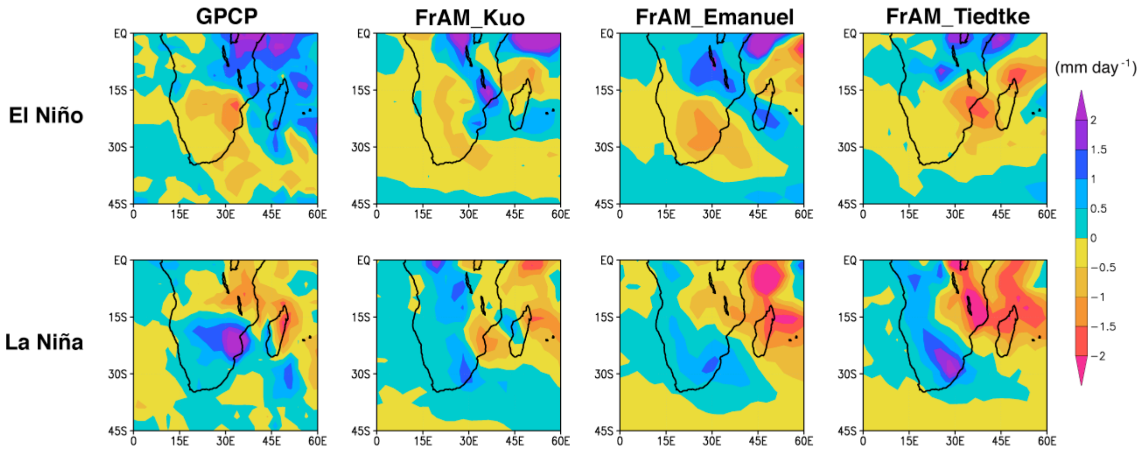

Figure 17: Composite of precipitation anomalies (in mm day^{-1}) in (upper panels) El Niño and (lower panels) La Niña years.

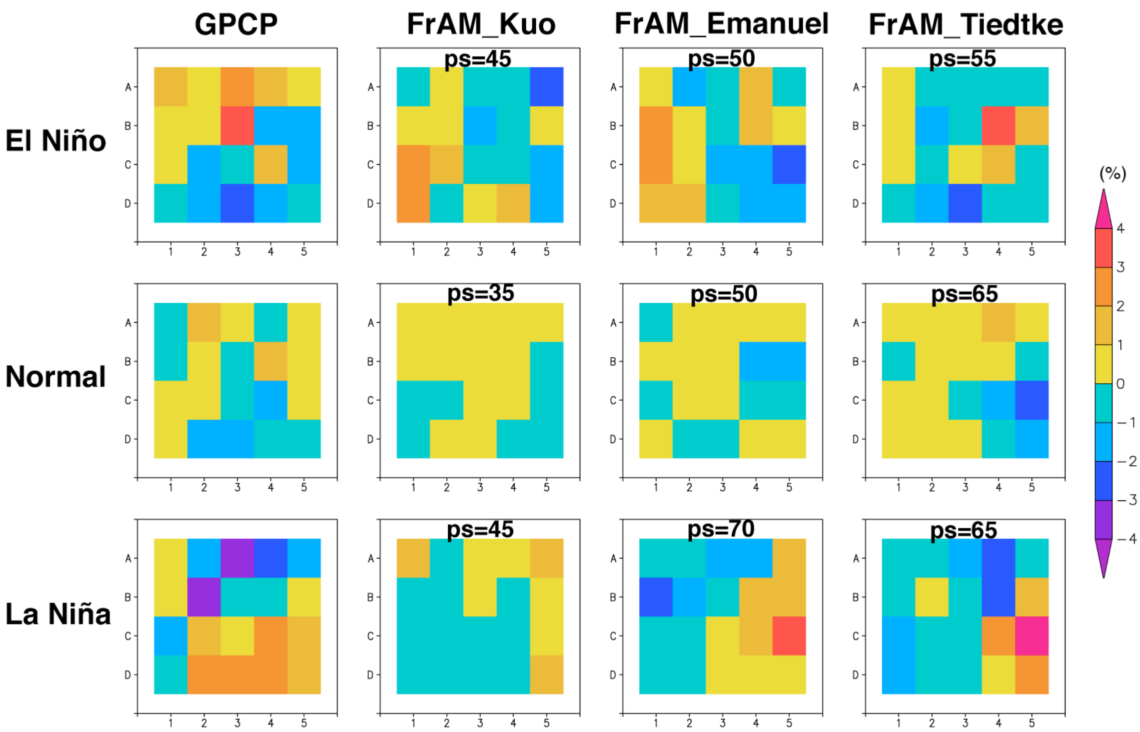

Figure 18: Frequency map of the SOM array showing how frequently each precipitation pattern appears during El Niño, normal, and La Niña years in the GPCP observation and three versions of FrAM. Here, deviations from the seasonal mean percentage are shown, and "ps" signifies phase synchronization.